

# Discrete Modular Serpentine Robotic Tail: Design, Analysis and Experimentation

Wael Saab\*, William S. Rone\*, and Pinhas Ben-Tzvi\*

\*Robotics and Mechatronics Laboratory, Department of Mechanical Engineering, Virginia Tech, Blacksburg, VA 24061, United States

**Email:** Wael Saab ([waelaab@vt.edu](mailto:waelaab@vt.edu)), William Rone ([wsrone@vt.edu](mailto:wsrone@vt.edu)), Pinhas Ben-Tzvi ([bentzvi@vt.edu](mailto:bentzvi@vt.edu))

**Corresponding author:** Pinhas Ben-Tzvi,  
Goodwin Hall Room 465  
635 Prices Fork Road (0238)  
Blacksburg, VA 24061  
Phone: (540) 231-6938

**Abstract:** This paper presents the design, analysis and experimentation of a Discrete Modular Serpentine Tail (DMST). The mechanism is envisioned for use as a robotic tail integrated onto mobile legged robots to provide a means, separate from the legs, to aid stabilization and maneuvering for both static and dynamic applications. The DMST is a modular two-degree-of-freedom (DOF) articulated, under-actuated mechanism, inspired by continuum and serpentine robotic structures. It is constructed from rigid links with cylindrical contoured grooves that act as pulleys to route and maintain equal displacements in antagonistic cable pairs that are connected to a multi-diameter pulley. Spatial tail curvatures are produced by adding a roll-DOF to rotate the bending plane of the planar tail curvatures. Kinematic and dynamic models of the cable driven mechanism are developed to analyze the impact of trajectory and design parameters on the loading profiles transferred through the tail base. Experiments using a prototype are performed to validate the forward kinematic and dynamic models, determine the mechanism's accuracy and repeatability, and measure the mechanism's ability to generate inertial loading.

**Keywords:** Mechanism Design, Robotic Tail, Cable-Driven Robot, Kinematics, Dynamics, Simulation

## 1. INTRODUCTION

By observing nature, engineers can gain a source of inspiration to address major challenges within the field of robotics. For instance, tails are commonly used by animals to assist in propulsion, stabilization, maneuvering, and manipulation<sup>1</sup>. Kangaroos have been observed to use their tails both as a counter balance and as an anchor point to provide a stable posture while standing on their hind legs<sup>2</sup>. Kangaroo rats have been observed to swing their tails in mid-air to reorient their bodies. Similarly, dinosaurs such as the Tyrannosaurus Rex are believed to have used their tails as a counter balance to stabilize their walking gait<sup>3,4</sup>. Lizards have also been observed to use their tails for aerial maneuvers to dynamically adjust their pose for smooth landing<sup>5,6</sup>. Other examples include a monkey using its tail to climb and grasp onto objects, a fish using its tail to provide propulsion, and an alligator using its tail for underwater rolling.

In the field of legged robotics, the dominant research paradigm has focused on leg mechanism design and control to propel, maneuver and stabilize the robot<sup>7</sup>. The authors believe that by using a spatial, articulated tail mechanism to aid in these functionalities onboard a legged mobile robot, the burden on the robot's limbs to simultaneously maneuver and stabilize the robot will be reduced. This could allow for simplification of the leg's control algorithms and/or the leg mechanism's design.

To address these challenges, the authors proposed a Discrete Modular Serpentine Tail (DMST) that is intended for the use on legged robots to augment performance. This paper builds on the authors' previous work<sup>8</sup> by further developing kinematic and dynamic models. These models are validated through a series of analytical and experimental case studies aimed to investigate the parameters that affect loading profiles and assess the performance of the mechanism. Simulations of the proposed mechanism attached to a planar biped robot modeled

analytically and using a commercial multibody dynamics package demonstrate the tail's performance enabling capabilities in disturbance rejection and quasi-static walking applications. The proposed work is part of ongoing research studying the design and implementation of a variety of robotic tails capable of augmenting a legged robot's ability for agile and robust terrain traversal in unstructured hazardous environments<sup>8-17</sup>.

The paper is organized as follows: Section 2 reviews prior work of inertial adjustment mechanisms, robotic tails and presents related work in the fields of continuum and serpentine robotics to highlight useful design criteria that have inspired the proposed mechanism. Section 3 presents the detailed design of the DMST. Section 4 provides a kinematic and dynamic model of the DMST. Section 5 presents a series of case studies that analyze the impact of trajectory and design parameters on loading profiles. Section 6 presents experimental results using a prototype to measure the mechanisms accuracy and repeatability and to demonstrate the systems performance in generating loading profiles. Section 7 presents case studies for utilizing this tail structure for disturbance rejection and stable walking on-board a planar biped robot. Section 8 presents concluding remarks and discusses future work.

## 2. RELATED WORK

This section reviews the technologies of inertial adjustment mechanisms and discusses the feasibility of such systems onboard mobile robots (Sec. 2.1) which then leads to a review of robotic tail mechanisms (Sec. 2.2). An overview of under-actuated mechanisms is then presented (Sec. 2.3) to discuss the design motivation of the proposed mechanism (Sec. 2.4).

### 2.1 Inertial Adjustment Mechanisms

Inertial adjustment mechanisms are defined by their ability to generate control forces and moments about their attachment point or adjust the system center-of-mass (COM). These mechanisms can be categorized based on their means of operation: 1) Substrate interaction mechanisms: propel a surrounding medium to produce forces and moments such as thrusters, gas jets, turbojets and turbofans<sup>18-19</sup>, 2) Translational mechanisms: displace a reaction mass to adjust the COM location<sup>20</sup>, 3) Rotational mechanisms: can be either symmetrical such as gyroscopes and reaction wheels<sup>21</sup> that produce a reaction torque or unsymmetrical such as a pendulum that produce reaction forces, moments and can adjust COM location.

Although category 1 mechanisms are highly capable inertial adjustment mechanisms, the requirement of compressors and fuel make practical implementation on board a mobile robot challenging. Similarly, the effectiveness of category 2 mechanisms relies on the translational stroke length of the reaction mass and may require a large foot print onboard a relatively compact mobile robot. Therefore, category 3 mechanisms will be further investigated.

Reaction wheels are compact in size and have extensive amounts of literature regarding their design and control; however, their performance is limited to mass and motor specifications<sup>22</sup>. Pendulums can be designed with larger inertia while maintaining a constant mass due to its quadratic relation with length but require a larger workspace and may interfere with the ground or robot during operation. Comparative analysis of the angular impulse between reaction wheels and robotic tails, in the form of rigid body pendulums, have indicated that a tail can produce significantly larger angular impulses in short time durations making it more appropriate when there is a sufficient workspace for implementation while reaction wheels can provide moments over longer duration times due to an infinite rotational stroke length<sup>23</sup>. These results make robotic tails more suitable for dynamic, inertial adjustment applications onboard mobile robots.

### 2.2 Robotic Tails

To facilitate a comparative analysis of prior research into robotic tails, a list of tail designs and their respective design criteria are shown in Table I. Many of these tails draw inspiration from biological structures as discussed in section 1 and cover a wide range of masses (17 to 2050 g) and lengths (73 to 500 mm). In terms of mechanical design, all the tails resemble single body rigid pendulums. Pitch degree-of-freedom (DOF) tails have been used for dynamic applications such as mid-air attitude control<sup>24-26</sup> and aiding the acceleration of mobile robots<sup>27</sup>. Yaw DOF tails have been used in dynamic applications involving maneuvering (turning)<sup>28, 29</sup> and propulsion<sup>30</sup>, and static applications to provide a counterbalance for stable walking of a bipedal robot<sup>31</sup>. Spatial, single body rigid pendulum tails have been proposed that greatly increase workspace and provide multi-axis enhanced performance capabilities at the cost of increased design complexity and control. These tails have been used for dynamic applications involving disturbance rejection<sup>32</sup>, mid-air attitude control<sup>32, 33</sup> and static stability applications on a quadruped robot<sup>34</sup>. Table 1 also shows that tails for static applications<sup>31, 34</sup> utilize low speed tail motions in the range of 1.3 – 6 rpm since accurate positioning of the tail mass is required, whereas the other tails utilize high speed tail motions to generate sufficient inertial loading.

Recent research has studied the effect of tail structures, ranging from a single body rigid pendulum to a 6 DOF articulated tail, on the yaw motion maneuverability of legged robots<sup>15</sup>. Results indicate that higher articulation results in larger angular displacements that corresponds to larger velocities and accelerations of the tail links that increase inertial loading in comparison to single body rigid pendulums undergoing equivalent tail motions. However, increased articulation requires more complex mechanical designs and control of the additional DOFs. Therefore, the authors aim to continue efforts in realizing an articulated tail structure via an open chain, under-actuated mechanism.

Table I. Comparison of Robotic Tail Designs and Physical Properties

Citation	[ <sup>24</sup> ]	[ <sup>25</sup> ]	[ <sup>26</sup> ]	[ <sup>27</sup> ]	[ <sup>28</sup> ]	[ <sup>29</sup> ]	[ <sup>30</sup> ]	[ <sup>31</sup> ]	[ <sup>32</sup> ]	[ <sup>33</sup> ]	[ <sup>34</sup> ]
Tail Tip Mass (g)	371	1000	17	400	70	400	~30	2050	400	70	-
Tail Length (mm)	177	500	103	500	102	500	85	150	500	73	100
Motor Power (W)	19	-	4	120	2.5	120	1	5.5	70 ea.	1.75	-
Tail Speed (rpm)	240	21	3000	~47	400	76	71	6	~22	320	1.3
Workspace (deg)	220	-	255	224	265	224	180	180	180/150	135/135	180/360
Mechanical Design	Planar								Spatial		
	Single Body Rigid Pendulum										

### 2.3 Design Candidates

The term under-actuation is used to describe a robotic system having fewer actuators than DOFs<sup>35</sup>. Examples from nature indicate that not all DOFs need to be independently actuated; for instance the human hand is estimated to have 21 DOF and is actuated with 16 muscle pairs via a complex tendon system located in the forearm<sup>36</sup>. This section will review the two main classes of under-actuated, open chain robots, continuum and serpentine, to identify design challenges and highlight useful design criteria that have inspired the DMST.

Continuum robots are characterized by their ability to continuously bend along their length similar to tentacles, tongues, and tails found in nature<sup>37</sup>. Several forms of these robots have been investigated and can be classified according to their method of actuation<sup>38</sup>. Intrinsically actuated designs combine both the actuators and supporting structure into one unit where motion is produced through the expansion or contraction of parallel bellows<sup>39</sup>, electrostrictive polymer artificial muscles<sup>40</sup>, and shape memory alloys<sup>41</sup>. Extrinsically actuated designs utilize remote actuation transmitted to the robot, often using cables or rods<sup>42</sup> and a compliant backbone to regulate angle distribution. This form of actuation enables miniaturization of the manipulator cross section and volume. Continuum robots have been proposed for use in congested environments such as search and rescue operations<sup>43</sup>,<sup>44</sup> and medical applications involving diagnosis and surgery<sup>45,46</sup>. Although they are capable of forming articulated spatial curvatures, on the macro-scale, their elasticity results in significant sagging due to gravity that poses difficulties in modeling kinematics; furthermore, the absence of conventional joints, rotary or linear, poses challenges in sensing configuration using techniques such as robot vision, magnetic sensors, strain deformation sensors, optical fibers, inertial measurement units, actuation force and cable displacement monitoring<sup>10,12,47</sup>.

Serpentine robots are rigid-link robotic systems composed of a large number of links interconnected with revolute joints in parallel or skewed configurations capable of forming discretized planar curvatures (for parallel joints) or spatial curvatures (for skewed joints)<sup>48</sup>. The application area in serpentine robotics is snake-like locomotion<sup>49-51</sup>. Unlike continuum robots, the kinematics of these mechanisms can be modeled using conventional rigid-body techniques. Conventional designs often utilize intrinsic actuation where an actuator is mounted onto each joint located along the length of the robot. However, these designs result in increased manipulator mass and actuator load requirements. Another approach utilizes a cable transmission system where the actuators are located away from the manipulator structure. Such mechanisms utilize a compliant core<sup>52-54</sup> to distribute equal angular rotation or specially designed rolling contact joints<sup>55</sup> to maintain equal antagonistic cable displacements that enable the connection of two active cables to one pulley; therefore requiring one actuator and further reducing weight and control complexity of the overall robotic system. The merits of cable driven serpentine-like mechanisms have widely been used in applications such as robotic hand/finger designs<sup>56,57</sup> that utilize friction pulleys<sup>58</sup>, higher order rolling pairs<sup>59</sup>, and spring-loaded joints<sup>60</sup> to regulate angle distribution.

## 2.4 Design Specifications

Based on the reviews in sections 2.1-2.3, it is desirable for a tail to be spatial, for increased workspace and capable of influencing multiple axis, and articulated in structure with a relatively few number of actuators controlling its motion. The tail should be designed for both static and dynamic applications for accurate COM positioning and high-speed tail motions to generate sufficient loading about its base. These design specifications enable the response to a multitude of situations such as stabilization, disturbance rejection, and maneuvering.

A robotic tail with a serpentine structure is chosen to construct the robotic tail due to its conventional means of mechanical design, modeling and sensing. Extrinsic actuation transmitted by cables is chosen to actuate the robotic tail for the following reasons: 1) actuators can be mounted at the tail base to reduce actuator loads during high speed motions, 2) a robust cable routing scheme enables controllable motions of articulated, under-actuated mechanisms<sup>61</sup> and 3) a cable transmission system with a tensioning system exhibits little backlash.

The mechanical structure and cable routing scheme determines the system's required number of active DOFs for controlled motions. For example, Fig. 1(a) shows a single link with a revolute joint located at its base that is actuated using a straight cable routing scheme. Left and right cable displacements ( $\Delta_L$  and  $\Delta_R$ , respectively) are calculated using Eq. 1, where  $R$  is the effective radius/length of the link, and  $\{h, w, \alpha\}$  are the geometric link parameters shown in Fig. 1(a). Since antagonistic cable displacements are not equal in magnitude for a given link rotation  $\theta$ , each cable requires an independent actuator and control scheme to produce rotation.

$$\begin{aligned}\Delta_L &= \sqrt{h^2 + w^2 - 2hw\cos(\alpha - \theta)} - R, \\ \Delta_R &= \sqrt{h^2 + w^2 - 2hw\cos(\alpha + \theta)} - R\end{aligned}\quad (1)$$

Figure 1(b) shows a straight cable routing method employed by manipulators that utilize an elastic core for angle regulation. Due to material isotropy, it can be assumed that bending is uniform<sup>52-54</sup>. Therefore, the mechanism can be modeled as two links rotating about a centered revolute joint. The associated  $\Delta_L$  and  $\Delta_R$  are defined in Eq. 2 with the geometric parameters  $\{w, R\}$  defined in Fig. 1(b). For small rotations antagonistic cable displacement can be assumed to be equal and opposite and can be attached to a single driving pulley; thus, reducing the overall size, weight and control complexity of the cable driven mechanism<sup>53</sup>. However, for large deflections each cable requires an actuator and synchronous control that may increase the size and complexity of the system<sup>52, 54</sup>.

$$\begin{aligned}\Delta_L &= -2w\sin(\theta/2) - 2R\sin^2(\theta/4), \\ \Delta_R &= 2w\sin(\theta/2) - 2R\sin^2(\theta/4)\end{aligned}\quad (2)$$

To address these challenges, the proposed design will investigate the effectiveness of grooved, cylindrical contoured links that act as pulleys to route cables and maintain equal cable displacements with minimal slack during operation. The cylindrical routing scheme, shown in Fig. 1(c), results in the equal but opposite left and right cable displacements defined in Eq. 3 using the  $R$  geometric parameter defined in Fig. 1(c). Therefore, if the antagonistic cables are initially tensioned and connected to a pulley, the cylindrical routing method can ensure no cable slack during rotation of the pulley. This design feature enables antagonistic cables from multiple links to be attached to a single multi-diameter pulley that can be actuated using a single motor, thus reducing the number of actuators required to achieve tail curvatures, as further discussed in section 3.

$$\Delta_L = R\theta, \quad \Delta_R = -R\theta \quad (3)$$

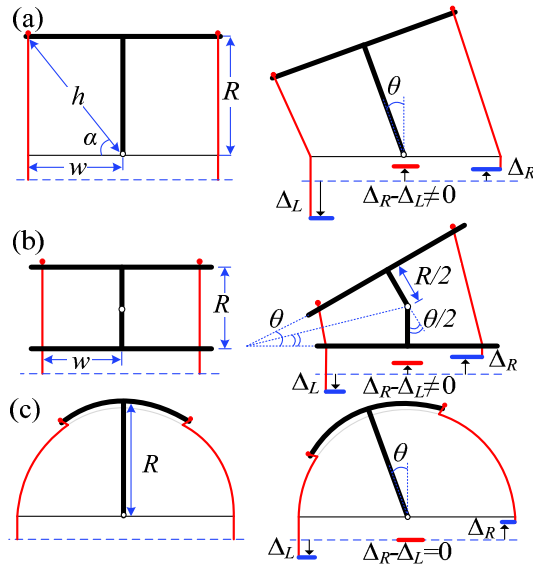


Fig. 1. Various mechanical structure and cable routing approaches: (a) Base located revolute joint with straight cable routing, (b) Uniform bending of a centered revolute joint with straight cable routing, (c) cylindrical cable routing.

### 3. MECHANICAL DESIGN

This section presents the mechanical design of the DMST, where the design specifications from section 2 are implemented in the proposed mechanism.

Figure 2 presents a simplified schematic diagram of the proposed mechanism showing the actuation unit and two tail links. The tail structure is composed of a series of links connected to one another using parallel revolute joints and to ground through a revolute joint that is perpendicular to the other joints. The mechanism is capable of controlling two-DOF: 1) roll about the ground y-axis that changes the orientation of the bending plane to distribute loading, and 2) tail bending in the actuation unit x-y plane that varies the tail COM location and generates loading profiles via high-speed tail motions. The roll-DOF  $\phi$  is actuated directly using a high-torque servomotor, and the bending-DOF is actuated using a cable transmission system driven by a high torque servo motor that rotates a multi-diameter pulley (MDP) by an angle  $\theta$ . The motors and MDP are located within the actuation unit that serves as a protective, rigid housing for electrical components and distributes routed cables to their respective pulley diameters.

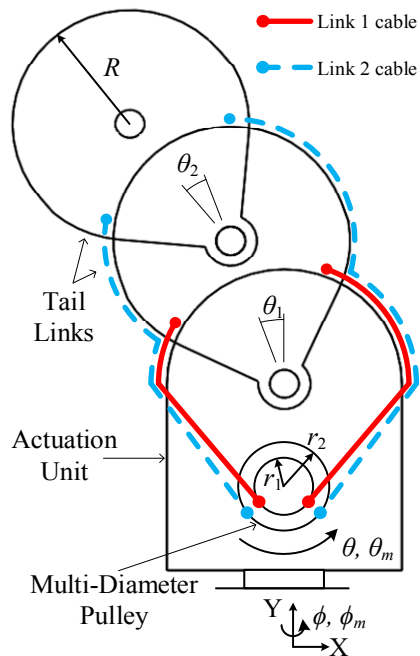


Fig. 2. Simplified schematic diagram and kinematic model of a two-link DMST.

As shown in Fig. 2, each link is connected to the MDP using an antagonistic pair of low-friction, nylon coated steel braided cables with swaged ball bearings to secure the cable ends. The cables terminating at each link route through mid-links that separate the link at which the cables terminate and the actuation unit. A mid-link, such as link 1 in Fig. 2, is a link that has two or more cables routed through it that do not terminate at that particular link. Mid-links have a grooved, cylindrical surface that is used for cable routing to maintain equal cable displacements as the MDP is rotated as discussed in section 2.

Figure 3(a) shows the detailed mechanical design of a 3-link DMST. Tail links are designed to be lightweight, rigid structures capable of tolerating high loads produced by cable tension. The MDP consists of  $n$  grooved channels used for routing and terminating cables that control the positioning of  $n$  links. The maximum number of links the DMST structure can accommodate is dependent on geometric constraints required for the MDP grooved channel widths. Furthermore, additional links requires more routed cables that increase friction in the structure a concept that will be modeled and evaluated in sections 4 and 6 respectively. Varying the pulley diameter for each cable channel varies the net bending of the link at which that cable terminates; as a result, the desired tail bending motion can be achieved through the rotation of a single DOF. Previous work has presented an optimization procedure to compute mechanism dimensions to achieve a desired set of best fit tail curvatures<sup>8</sup>.

A pair of tensioning systems are built into the two sides of each tail link (Fig. 3(b)). These are used to tension routed antagonistic cables to maintain a straight home configuration, keep cables routed along their cylindrical contours, and minimize backlash during operation. The tensioner consists of a sliding unit that is capable of translating within a slot using a screw and nut mechanism. Tightening the screw translates the sliding unit inward. With sufficient translation, the sliding unit engages and tensions the routed cables, which causes an angular adjustment of the link. Cable tensioning is performed on both sides of each link to align its orientation. The tensioning procedure is initiated at the lowest link and ends at the  $n$ -th link since the rotation of links nearer the base affect the orientation downstream due to the serial structure.

A flat link is placed at the end of the tail to serially connect DMST units. For example, Fig. 3(c) shows a robotic tail concept consisting of two 5-link DMSTs connected in series forming planar S- and U-shaped tail curvatures. If the tail is performing manipulation tasks, modular end effectors such as a robotic gripper can be attached to the end link to improve the tail's functionality. Spatial configurations can be achieved using the roll DOFs. The concept of modularity to enhance manipulation through the serial connection of DMSTs presents the authors' future envisionment of this mechanism to move beyond the paradigm in which a robotic tail is used for one function on board a mobile robot. However, this concept will be further investigated in future work as discussed in section 8.

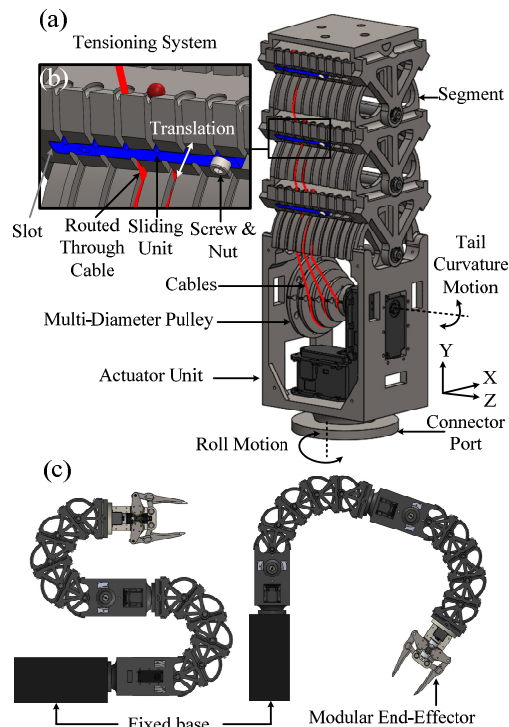


Fig. 3. (a) Mechanical design of a 3-link DMST, (b) Close up view of a mid-link and tensioning system, (c) Planar S- and U-shaped curvatures of two five-link DMSTs connected in series.

## 4. MECHANICS MODELING

This section presents a mathematical model for the DMST. After analyzing the kinematic coupling created in the mechanism by the actuation cabling, the kinematics and dynamics of the mechanism are derived.

### 4.1 Joint Angle Trajectories

The actuation cabling between the MDP and links creates a kinematic coupling between the MDP rotation and each link's joint angle (assuming the cable is inextensible). However, the cable routing for link  $i > 1$  will route along the previous  $i-1$  links. Therefore, the cable path length change due to these joint angles must be considered.

Equation 4 recursively maps the prescribed MDP angle  $\theta_m$  into the joint angles  $\theta_i$ , where  $\eta_i$  (defined in Eq. 5) is the coupling ratio between  $r_i$ , the MDP radius for the cable terminating at link  $i$ , and  $R$ , the radius of the circular cable routing surfaces. These parameters are shown in Fig. 2 for a two-link DMST. The roll joint angle  $\phi$  equals the prescribed motor angle  $\phi_m$  due to direct drive, also defined in Eq. 4. The associated joint velocities  $\dot{\phi}$  and  $\dot{\theta}_i$  and accelerations  $\ddot{\phi}$  and  $\ddot{\theta}_i$  may be found by differentiating Eq. 4.

$$\theta_i = \begin{cases} \eta_i \theta_m & i = 1 \\ \eta_i \theta_m - \sum_{j=1}^{i-1} \theta_j & 1 \leq i \leq n \end{cases} \quad (4)$$

$$\phi = \phi_m$$

$$\eta_i = r_i / R \quad (5)$$

### 4.2 Position, Velocity and Acceleration Kinematics

Kinematic illustrations of the base link (link 0), intermediate links (links 1 through  $n-1$ ), and terminal link (link  $n$ ) are shown in Fig. 4, with relevant frame and kinematic parameters used in this analysis defined graphically. Subscript  $D$  denotes vectors or matrices defined in the DMST frame of reference. This notation will help in differentiating variables in the legged robot frame that will be introduced in section 7.

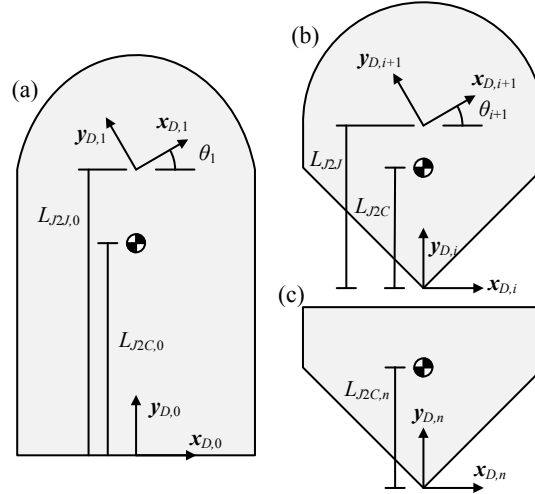


Fig. 4. Kinematic illustrations of DMST links: (a) base link 0, (b) intermediate link 1- $n$ , (c) terminal link  $n$ .

The link  $i$  orientation matrix  $\mathbf{R}_{D,i}$  is defined in Eq. 6, where  $\mathbf{R}_Y(\phi)$  is a y-axis rotation by angle  $\phi$  and  $\mathbf{R}_Z(\theta_i)$  is a z-axis rotation by angle  $\theta_i$ . The body 0 rotation is due to the roll of link 0 with respect to the tail base frame, and the body  $i$  rotation is due to the pitch of link  $i$  with respect to link  $i-1$ .

$$\mathbf{R}_{D,i} = \begin{cases} \mathbf{R}_Y(\phi) & i = 0 \\ \mathbf{R}_{D,i-1} \mathbf{R}_Z(\theta_i) & 1 \leq i \leq n \end{cases} \quad (6)$$

As shown in Fig. 4, the positions of the tail's joint centers  $\mathbf{p}_{D,jnt,i}$  and link COM  $\mathbf{p}_{D,COM,i}$  are calculated using Eqs. 7-8, where  $L_{J2J,0}$  is the distance from the roll joint to pitch joint 1,  $\mathbf{y}$  is the y-axis unit vector,  $L_{J2J}$  is the distance between adjacent pitch joints,  $L_{J2C,0}$  is the distance from joint 0 to the link 0 COM,  $L_{J2C}$  is the distance between an intermediate link's pitch joint and COM, and  $L_{J2C,n}$  is the distance between joint  $N$  and the link  $n$  COM.

$$\mathbf{p}_{D,jnt,i} = \begin{cases} 0 & i = 0 \\ \mathbf{p}_{D,jnt,i-1} + L_{J2J,0} \mathbf{R}_{D,i-1} \mathbf{y} & i = 1 \\ \mathbf{p}_{D,jnt,i-1} + L_{J2J} \mathbf{R}_{D,i-1} \mathbf{y} & 2 \leq i \leq n \end{cases} \quad (7)$$

$$\mathbf{p}_{D,COM,i} = \begin{cases} \mathbf{p}_{D,jnt,i} + L_{J2C,0} \mathbf{R}_{D,i} \mathbf{y} & i = 0 \\ \mathbf{p}_{D,jnt,i} + L_{J2C} \mathbf{R}_{D,i} \mathbf{y} & 1 \leq i \leq n-1 \\ \mathbf{p}_{D,jnt,i} + L_{J2C,n} \mathbf{R}_{D,i} \mathbf{y} & i = n \end{cases} \quad (8)$$

Link  $i$  angular velocities  $\boldsymbol{\omega}_{D,i}$  are defined in Eq. 9, where  $\mathbf{z}$  is the z-axis unit vector.

$$\boldsymbol{\omega}_{D,i} = \begin{cases} \dot{\phi} \mathbf{R}_{D,i} \mathbf{y} & i = 0 \\ \boldsymbol{\omega}_{D,i-1} + \dot{\theta}_i \mathbf{R}_{D,i} \mathbf{z} & 1 \leq i \leq n \end{cases} \quad (9)$$

### 4.3 Actuation Loading Requirements

For this robotic structure, three sources of loading are considered: inertia, gravity and actuation. The inertial force  $\mathbf{F}_{D,inr,i}$  and moment  $\mathbf{M}_{D,inr,i}$  and gravitational force  $\mathbf{F}_{D,grv,i}$  acting at each link  $i$  COM as external loading, while the actuation contributes to the joint moment  $\mathbf{M}_{D,jnt,i}$  as discussed below. Because the joint angles are prescribed, the kinematics, the inertial loading can be directly calculated from the applied trajectories; the only unknowns are the joint forces  $\mathbf{F}_{D,jnt,i}$  and moments  $\mathbf{M}_{D,jnt,i}$ .

Figure 5 illustrates free body diagrams for the terminal link and an intermediate link of the DMST. A recursive formulation of the equations of motion (starting from the  $n$ -th link and propagating to  $n = 0$ ) based on these free body diagrams are defined in Eq. 10, where  $\mathbf{p}_{D,CJ,i,j}$  is the position vector from the link  $i$  COM to joint  $j$ , defined in Eq. 11. The notation  $\tilde{\mathbf{a}}\mathbf{b}$  denotes  $\mathbf{a} \times \mathbf{b}$ .

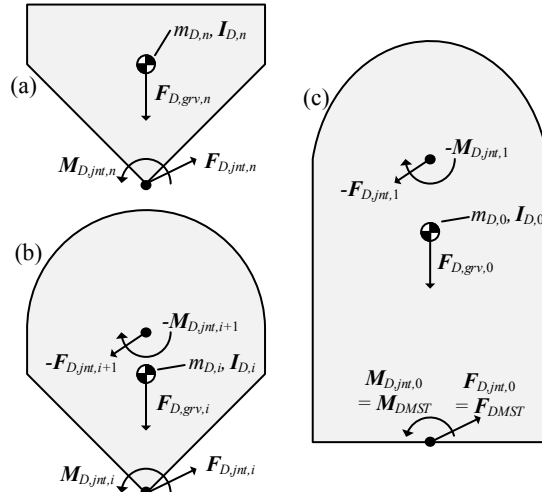


Fig. 5. Free body diagrams of DMST links: (a) terminal link  $n$ , (b) intermediate link  $i$ , (c) base link  $0$ .

$$\mathbf{F}_{D,inr,i} = \begin{cases} \mathbf{F}_{D,jnt,i} + \mathbf{F}_{D,grv,i} & i = n \\ -\mathbf{F}_{D,jnt,i+1} + \mathbf{F}_{D,jnt,i} + \mathbf{F}_{D,grv,i} & 0 \leq i \leq n-1 \end{cases} \quad (10)$$

$$\mathbf{M}_{D,inr,i} = \begin{cases} \mathbf{M}_{D,jnt,i} + \tilde{\mathbf{p}}_{D,CJ,i,i} \mathbf{F}_{D,jnt,i} & i = n \\ -\mathbf{M}_{D,jnt,i+1} + \mathbf{M}_{D,jnt,i} - \tilde{\mathbf{p}}_{D,CJ,i,i+1} \mathbf{F}_{D,jnt,i+1} + \tilde{\mathbf{p}}_{D,CJ,i,i} \mathbf{F}_{D,jnt,i} & 0 \leq i \leq n-1 \end{cases}$$

$$\mathbf{p}_{D,CJ,i,j} = \mathbf{p}_{D,jnt,j} - \mathbf{p}_{D,COM,i} \quad (11)$$

These equations of motion may be reorganized into recursive formulations of joint load forces  $\mathbf{F}_{D,jnt,i}$  defined in Eq. 12, where  $m_{D,i}$  is the link  $i$  mass and  $g$  is gravitational acceleration.

$$\mathbf{F}_{D,jnt,i} = \begin{cases} m_{D,i} (\ddot{\mathbf{p}}_{D,COM,i} - \mathbf{a}_{grv}) & i = n \\ \mathbf{F}_{D,jnt,i+1} + m_{D,i} (\ddot{\mathbf{p}}_{D,COM,i} - \mathbf{a}_{grv}) & 0 \leq i \leq n-1 \end{cases}, \quad \mathbf{a}_{grv} = -g\mathbf{y} \quad (12)$$

Equation 13 defines the recursive formulation of joint load moments  $\mathbf{M}_{D,jnt,i}$ , for which  $\mathbf{M}_{D,inr,i}$  is defined in Eq. 14. In Eq. 14,  $\mathbf{I}_{D,i}$  is the link  $i$  moment of inertia with respect to the ground frame, and  $\mathbf{I}_{D,i,lcl}$  is the link  $i$  moment of inertia with respect to the link  $i$  frame. The subscript  $lcl$  is used to identify the constant inertia tensor defined in the local body-fixed frame.

$$\mathbf{M}_{D,jnt,i} = \begin{cases} \mathbf{M}_{D,inr,i} - \tilde{\mathbf{p}}_{D,CJ,i,i} \mathbf{F}_{D,jnt,i} & i = n \\ \mathbf{M}_{D,inr,i} + \mathbf{M}_{D,jnt,i+1} + \tilde{\mathbf{p}}_{D,CJ,i,i+1} \mathbf{F}_{D,jnt,i+1} - \tilde{\mathbf{p}}_{D,CJ,i,i} \mathbf{F}_{D,jnt,i} & 0 \leq i \leq n-1 \end{cases} \quad (13)$$

$$\mathbf{M}_{D,inr,i} = \mathbf{I}_{D,i} \dot{\boldsymbol{\omega}}_{D,i} + \tilde{\boldsymbol{\omega}}_{D,i} \mathbf{I}_{D,i} \boldsymbol{\omega}_{D,i}, \quad \mathbf{I}_{D,i} = \mathbf{R}_{D,i} \mathbf{I}_{D,i,lcl} \mathbf{R}_{D,i}^T \quad (14)$$

The defining property of a revolute joint is that it cannot support a moment along its axis of rotation. Therefore, for each revolute joint  $i$ , the actuation loading must provide the moment in  $\mathbf{M}_{D,jnt,i}$  aligned with the revolute joint axis of rotation. The actuation loading differs for joint 0 and joints 1- $n$ . For joint 0, the revolute joint axis is  $\mathbf{R}_{D,0} \mathbf{y}$ , and the moment about this axis is a torque  $\tau_r$  directly provided by the roll-DOF gear motor output shaft, defined in Eq. 15.

$$\tau_r = (\mathbf{R}_{D,0} \mathbf{y})^T \mathbf{M}_{D,jnt,0} \quad (15)$$

For joints  $i = 1-n$ , the revolute joint axis is defined as  $\mathbf{R}_{D,i} \mathbf{z}$  and the moment along this axis is due to the cable tensions acting between links  $i-1$  and  $i$ . For an  $n$ -link DMST, there will be  $n$  cable tensions contributing to this moment, and the normal distance from the revolute joint to these tensions is  $R$ , resulting in the cable tension formulation in Eq. 16, where  $T_{i,j}$  is the tension at joint  $i$  of the cable terminating at link  $j$ .

$$R \sum_{j=i}^n T_{i,j} = (\mathbf{R}_{D,i} \mathbf{z})^T \mathbf{M}_{D,jnt,i} \quad (16)$$

For the cable tensions, assuming there is friction between the cable and tail structure along its length, recursive calculation of the cables' tensions from their termination point to the base is required. For a given  $j$ ,  $T_{i,j}$  will be non-zero only for  $i = [1, j]$ .

Solving for  $T_{i,j}$  consists of two steps performed recursively from joint  $i = n$  to joint  $i = 1$ : 1) calculating the  $T_{i,i}$  tension using Eq. 17, and 2) back-propagating the joint  $i$  tensions to joint  $i-1$  using Eq. 18, where  $\mu$  is the coefficient of friction and  $\chi_i$  is the contact angle between the cable and routing surfaces. Equation 17 was derived from Eq. 16 knowing that  $T_{i,j} = 0$  for all  $j < i$ , and Eq. 18 was found using a belt-friction model for the contact between the cable and routing surfaces between joints.

$$RT_{i,i} = \begin{cases} (\mathbf{R}_{D,i} \mathbf{z})^T \mathbf{M}_{D,jnt,i} & i = n \\ (\mathbf{R}_{D,i} \mathbf{z})^T \mathbf{M}_{D,jnt,i} - R \sum_{j=i+1}^n T_{i,j} & 1 \leq i \leq n-1 \end{cases} \quad (17)$$

$$T_{i,j} = \exp(\mu \chi_{i+1}) T_{i+1,j} \quad \forall j \geq i \quad (18)$$

The torque  $\tau_s$  required to drive the MDP may be calculated using Eq. 19, which takes the sum of the moments due to each cable tension acting over that cable's pulley radius.

$$\tau_s = \sum_{i=1}^n (r_i T_{0,i}) \quad (19)$$

## 5. DYNAMIC TAIL LOADING

Beyond understanding the actuation requirements of the DMST, the dynamic model should also be capable of calculating the loading (force and moment) the DMST applies through its roll joint.

The recursive calculations of  $\mathbf{F}_{D,jnt,i}$  and  $\mathbf{M}_{D,jnt,i}$  accumulate the loading due to the links' inertial and gravitational loading from the tip to the actuation module. Therefore, using the joint loading at link 0, the tail base loading  $\mathbf{F}_{DMST}$  and  $\mathbf{M}_{DMST}$  may be calculated using Eq. 20. The ground frame in which the tail model is defined is assumed to be located at the attachment point between the tail and legged structure.

$$\mathbf{F}_{DMST} = \mathbf{F}_{D,jnt,0}, \quad \mathbf{M}_{DMST} = \mathbf{M}_{D,jnt,0} \quad (20)$$

In the following analysis, the dynamic model of the DMST, developed in section 4, is used to simulate the system actuated with PID controlled servo motors. Experimentally measured data of the servo plant parameters including inertia, friction, damping and torque/speed saturations were extracted from <sup>62</sup> and controller gain coefficients were tuned for near-critical operation on the bases of empirical analysis. The dynamics of the system were used to evaluate Eq. 20. A five-link DMST is considered where  $L_{J2J} = 60$  mm,  $R = 25$  mm,  $r_i = [9, 16, 22, 28,$

34] mm and mass properties are held constant unless otherwise stated. Mass properties are estimated from a detailed CAD model shown in Figure 3. The link COM is assumed to be centered at its upper revolute joint and cable friction is neglected since low friction nylon coated cables are used on the prototype.

### 5.1 Trajectory – Inertial Analysis

Tail loading profiles are influenced by both static loading (gravity) and dynamic loading (inertia). Since gravitational effects are time-invariant (do not depend on velocity or acceleration), they are the same for a prescribed tail trajectory regardless of the tail motion’s time span. However, inertial effects are time-variant since greater accelerations correspond to greater magnitude loading profiles. Therefore, the inertial loading acts as perturbation to the steady-state gravitational loading. In this analysis, only planar bending is considered where  $\theta_m$  is varied from 0 to  $\pi/2$  rad to simulate a servo step response with various time spans, representing the duration of tail motion, to study its effect on inertial loading. Figure 6 presents the force and moments loading diagrams for the three time span case studies  $t = \{0.2, 0.3, 0.4\}$  sec. The time span of 0.2 sec represents the fastest step response the system can achieve the target position with PID gains set to  $K_p = 60$ ,  $K_i = 10$ , and  $K_d = 0.4$ . Time spans were elongated by reducing the proportional gain constant. To better visualize the perturbations from equilibrium, steady state gravitational force offsets about the y-axis were set to zero.

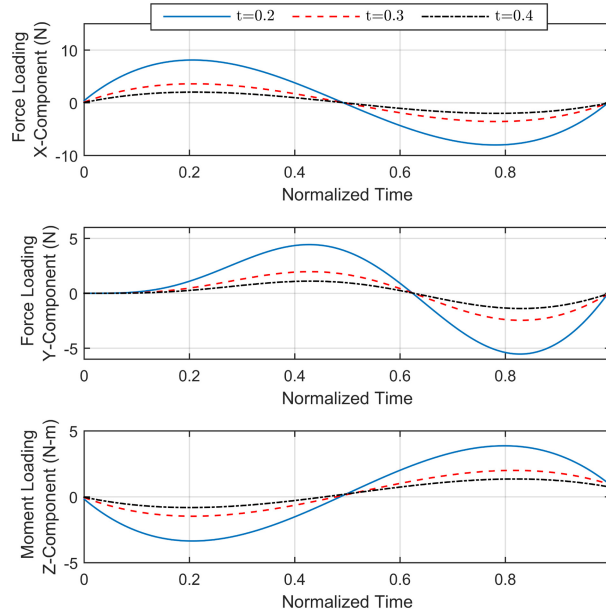


Fig. 6. Inertial analysis: computed loading profiles for  $t = \{0.2, 0.3, 0.4\}$  sec. The x-axis time is normalized as a fraction of the total duration to aid comparison.

It is observed from these plots that force loading profiles magnitudes: 1) increase as the time span decreases for each tail motion due to greater accelerations, and 2) approach a steady state profile as time spans increase due to the time invariance of gravitational effects. It is also noted that x- and y-components of the force loading at the endpoints are zero because these instances represent static configurations with zero velocities and accelerations; however, the final z-component moment loading is offset due to the gravitational induced moment at the tail’s end configuration.

### 5.2 Trajectory – Roll Angle

In section 5.1, a planar case study was analyzed in which the time span of the tail’s bending motion was varied. However, roll angle is another trajectory parameter that can be varied to distribute loading. In this analysis, simulations are performed using the 0.2 sec time span tail trajectories (similar to motion used in section 5.1) where the roll angle is varied at constant values  $\phi = \{\pi/4, \pi/2, 3\pi/4\}$  rad.

Figure 7 illustrates the associated loading results. Due to the rotational symmetry of the tail motions about the y-axis, the loading with respect to this axis (i.e., the y-components of force and moment) is invariant to the change

in  $\phi$ . Furthermore, since the tail is performing tail curvature motions at constant roll angles, the y-component moment loading is zero.

The x- and z-components show the impact of roll angle on the distribution of the loading profiles. For  $\phi = \pi/4$  and  $3\pi/4$  rad, x-component force and z-component moment profiles are equal and opposite, whereas the x-component moment and z-component force are equal in these two cases.

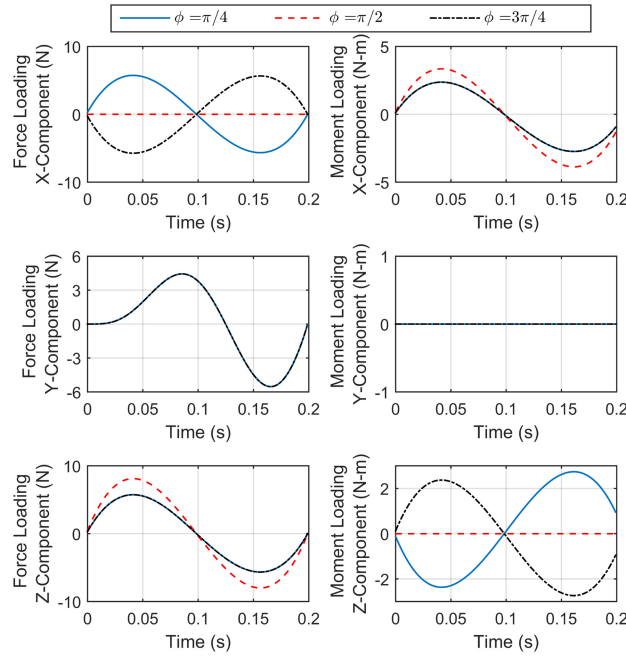


Fig. 7. Roll angle analysis: computed loading profiles for  $\phi = \{\pi/4, \pi/2, 3\pi/4\}$  rad.

### 5.3 Design – Mass Distribution Analysis

In addition to trajectory parameters, a tail’s design properties also impact the dynamic loading. Two design factors will be analyzed in this paper: mass distribution and coupling ratio. All design parameter analysis will use tail curvature motion with a 0.2 sec time span (similar to motion used in section 5.1).

The DMST is designed to accommodate a tip mass to increase the loading capacity for a given tail motion. This section analyzes the effects of the mass distribution ratio  $\beta$  on loading profiles, where  $\beta$  represents the ratio between an additional tip mass and the total weight of the tail (links and actuation unit). In this analysis, the total weight of the five-link DMST is 4.3 kg. All other design variables and properties are held constant to compare results with inertial analysis loading profiles.

Three case studies are presented in Fig. 8 that show force loading profiles where the mass distribution ratio is varied between three values  $\beta = \{0.5, 1, 1.5\}$  representing an additional tip mass equivalent to  $\{2.1, 4.3, 8.6\}$  kg attached to link 5.

Results indicate a linear correlation between the increase of tip mass and loading profiles magnitudes. In comparison to inertial analysis results with no tip mass, loading profile magnitudes increase approximately by factors of 3.2, 5.5, and 7.8 for  $\beta$  equal to 0.5, 1, and 1.5 respectively.

Although increasing tip mass generates larger magnitude dynamic force loading profiles, a maximum limit of additional tip mass is imposed by motor specifications. Using Eq. 19, the MDP torque requirements were computed for the  $\beta$  values under consideration, with results shown in Fig. 9. It is observed that the required torque for all case scenarios initially take on positive values to overcome inertia to move the tail in the positive orientation, then changes to negative values and attains maximum magnitudes during the deceleration phase then remains offset in this region due to gravitational loading. Mass distribution parameters must be chosen based on MDP angular velocity and torque requirements to select a motor that is capable of producing a desired tail motion.

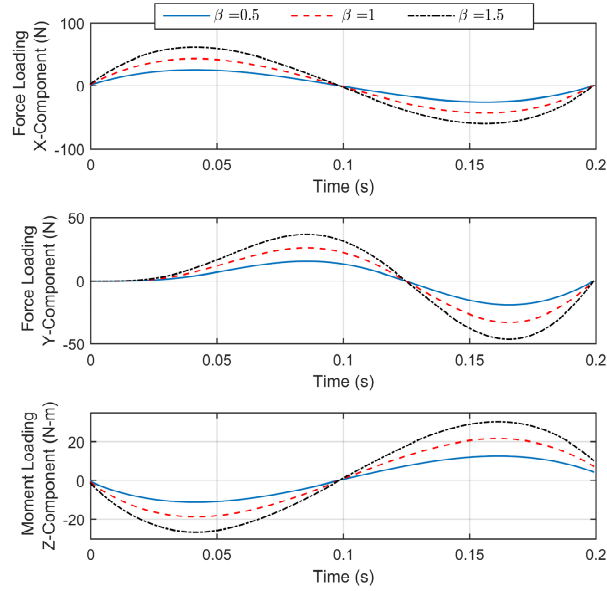


Fig. 8. Mass distribution analysis: computed loading profiles for  $\beta = \{0.5, 1, 1.5\}$ .

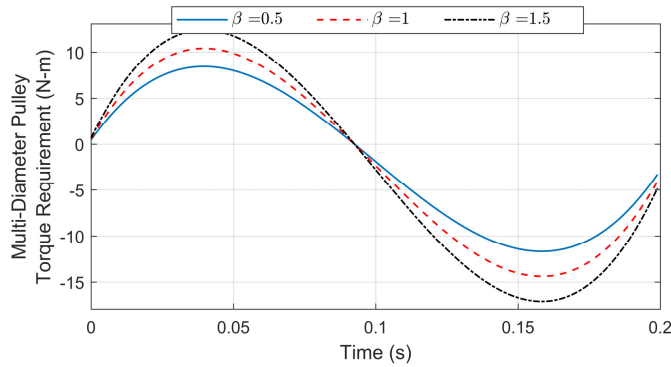


Fig. 9. Computed MDP torque requirements for  $\beta = \{0.5, 1, 1.5\}$ .

#### 5.4 Design – Coupling Ratio Analysis

The coupling ratio  $\eta_i$  is defined as the ratio between  $r_i$  and  $R$ , as discussed in section 4. This section will analyze the influence of the coupling ratios on loading profiles by varying MDP dimensions while maintaining a constant link circular routing curvature  $R = 25$  mm using a 0.2 sec tail curvature time span. Table II presents the design parameters of two case studies for various coupling ratios. Case 1 represents the scenario where MDP dimensions are scaled by a factor of 2 in comparison to dimensions used in section 5.1 and Case 2 represents the scaled, inverted scenario where the largest coupling ratios are connected to links adjacent to the actuation unit and decrease in progression to the tip of the tail (link 5).

Figure 10 shows the loading profile for the two case studies. By comparing peak values and with those from Fig. 6, the scaled coupling ratios in Case 1 have nonlinearly increased loading profiles. The x- and z-component loading increased by a factor of approximately 1.8 whereas y-component loading by a factor of 3.4. This nonlinear increase is expected due to the differentiation of trigonometric terms that are a function of link orientation given by Eq. 4 that yield accelerations multiplied by  $\eta_i^2$ . It is interesting to note that the inverted scenario Case 2, generates larger loading profiles than Case 1 since the higher coupling ratios of the tail bottom links correspond to a greater tail rotation and accelerations of the top links, thus producing larger dynamic loading. Greater tail rotations also correspond to a larger moment arm that produce a larger steady state gravitational moment about the z-axis.

Table II. Design parameters used for coupling ratio analysis

Case	$r_{1-5}$ (mm)	$\eta_{1-5}$
1	[18, 32, 44, 56, 68]	[0.7, 1.2, 1.7, 2.2, 2.7]
2	[68, 56, 44, 32, 18]	[2.7, 2.2, 1.7, 1.2, 0.7]

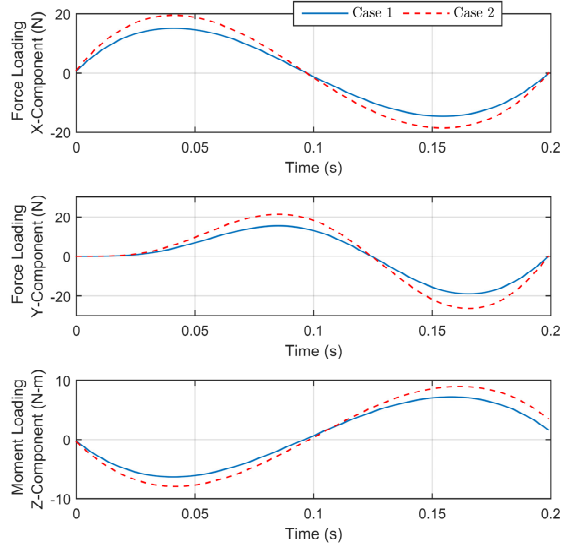


Fig. 10. Coupling ratio analysis: computed force and moment loading profiles.

## 6. EXPERIMENTAL RESULTS

In this section, experiments are performed using a five-link DMST prototype to validate forward kinematic relations, determine the mechanism's accuracy and repeatability, and measure the mechanism's ability to generate loading at its base.

Figure 11 shows the experimental test platform under consideration. The prototype's structural components were printed from ABS plastic. High torque servo motors rated for a stall torque of 10 N-m and no load speed of 55 rpm operated at an input voltage of 14 V drive the mechanism's two DOFs. Link lengths and pulley diameters were chosen to be  $L_{J2J} = 60$  mm  $R = 25$  mm, and  $r_i = [9, 16, 22, 28, 34]$  mm for  $i$  ranging from 1 to 5.

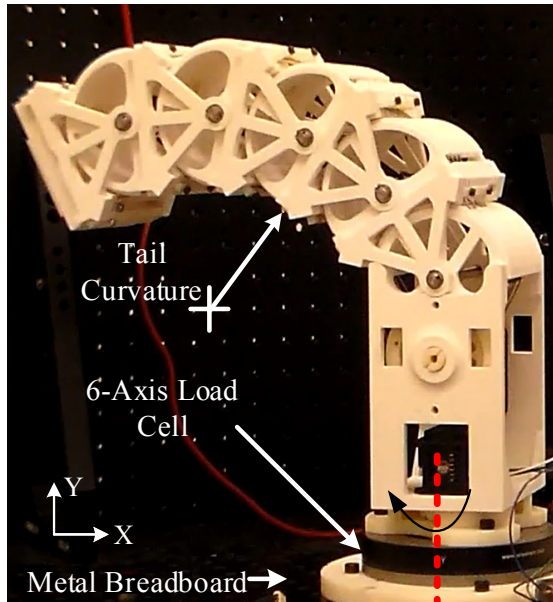


Fig. 11. Experimental setup of a five-link DMST prototype.

## 6.1 Forward Kinematics Experiment

A series of experiments were performed to validate the forward kinematic relations derived in section 4. The DMST was programmed to perform repeated cycles of three distinct tail curvatures: {C1, C2, C3} where the MDP angle is varied between  $\theta_m = \pm\{0, \pi/4, \text{ and } \pi/2\}$  rad respectively with a fixed° roll angle. The tail approached these curvatures in clockwise and counter clockwise sequences to determine if hysteresis due to cable friction and/or elasticity impacted performance. Tail curvatures were recorded using a high-resolution tracking camera mounted orthogonal to the tail curvatures. Image processing techniques were then implemented to measure the link orientations at each configuration. To test the mechanism's accuracy and repeatability, measurements were recorded for ten consecutive cycles. Table III presents the mean measured global orientation ( $\bar{\theta}_i$ ) and standard deviations ( $\sigma$ ) of the measured data and provides a comparison with link orientations computed using forward kinematics.

Table III. Measured experimental results and computed link orientations

LINK	MEASURED ORIENTATION CLOCKWISE SEQUENCE			COMPUTED ORIENTATION			MEASURED ORIENTATION COUNTER-CLOCKWISE SEQUENCE		
	$-\bar{\theta}_i \pm \sigma^\circ$			$\pm\theta_i^\circ$			$+\bar{\theta}_i \pm \sigma^\circ$		
	C1	C2	C3	C1	C2	C3	C1	C2	C3
1	0.4±0.1	11±0.3	22.2±0.2	0	10	20.1	0.5±0.6	10.4±0.3	22.2±0.4
2	0±0	16.5±0.5	33.1±0.6	0	16.5	33	0.4±0.5	15.9±0.5	34.4±0.1
3	-1.2±0.5	22.7±0.6	46.4±0.5	0	22.5	45	0.1±0.2	20.8±0.3	45.5±0.3
4	-1.2±0.2	28.3±0.4	59.3±0.3	0	28.4	56.9	1.6±0.8	28.5±0.3	59.2±0.5
5	0±0	33.8±0.7	70.4±0.3	0	34.4	68.9	0.5±0.4	31.2±0.2	67.3±0.4

From the Table III C1 measured orientations, it is observed that slight offsets are present at the home configuration. Although the tensioning procedure was performed, kinematic coupling creates difficulties in achieving a perfectly aligned home configuration since tensioning of one cable induces slight orientation changes in the remaining links. In addition, it was observed that a slight slack on one side of the cables, terminated at an identical link, is necessary to prevent the mechanism from locking up during operation. Lock ups result from highly tensioned cables for a link that prevent rotation in either direction. The counter-clockwise sequences fall on average  $-0.3^\circ$  below clockwise sequences. This result is expected because the steel braided cables used on the prototype are nylon coated and exhibit minimal friction and elasticity therefore the effects of hysteresis were unobservable from the data presented in Table III. From the measured standard deviation data, the maximum repeatability of the mechanism ranged between  $\pm 0.8^\circ$  for each link. Overall, measured angular orientations indicate close correlation with respect to computed orientations. On average, links 4 and 5 showed the largest deviations from computed orientations ranging from to  $2.3\text{-}3.1^\circ$ , due to the accumulation of error along the serial structure.

## 6.2 Loading Profile Measurements

In order to measure the generated loading profiles and verify the dynamic tail loading model presented in section 5, the five-link DMST prototype was connected to a six-axis load cell to measure the loading profiles generated by the tail, as shown in Figure 11. Sensor measurements were sampled at 400 Hz using a PCI data acquisition card. A moving window mean of 50 sample points was used to smooth the measured data.

In this experiment, the tail performed a tail curvature by sending a  $\pi/2$  rad goal angle at maximum angular velocity and torque to the servo motor controlling the MDP rotation. Loading profiles were measured for constant roll angles of  $\pi/4$ ,  $\pi/2$  and  $3\pi/4$  rad, similar to the case scenarios shown in Fig. 7.

Figure 12 illustrates the measured loading profiles for various roll angles. From the plot, it can be observed that tail curvature motion is completed in 0.24 s, after which the tail experiences vibrations that dissipate to steady state conditions. It is expected that friction within the mechanism extended the response time above the 0.2 s obtained from simulated results that assumed no cable friction  $\mu = 0$ . In comparison to computed results shown in Fig. 7, the measured loading profiles do exhibit similar distributed loads as the roll angle is varied: 1) y-component moment loading maintains a zero value for the three case scenarios, 2) y-component force loading is approximately invariant to roll, 3) x-component force and z-component moment profiles, for  $\phi = \pi/4$  and  $3\pi/4$  rad, are approximately equal and opposite, whereas the x-component moment and z-component force are approximately equal in magnitude, 4) steady-state gravitational moment offsets closely match computed results,

5) the profiles qualitatively match the shape of computed profiles but do not exactly match the smooth contours due to vibrations in the long structure during tail motions that have not been modeled analytically.

Measured peak loading profile values, equal to 6 N and 1.8 N-m, fall below computed values because the experimental tail motion duration was slightly longer than the 0.2 s time span used in computed results. This is expected since as the time spans of tail motions are lengthened, dynamic loadings decrease towards steady state gravitational loading conditions as explained in section 5. The results of this experiment will be used to update simulation parameters, in particular dissipative friction, to better compute loading profiles as part of future work.

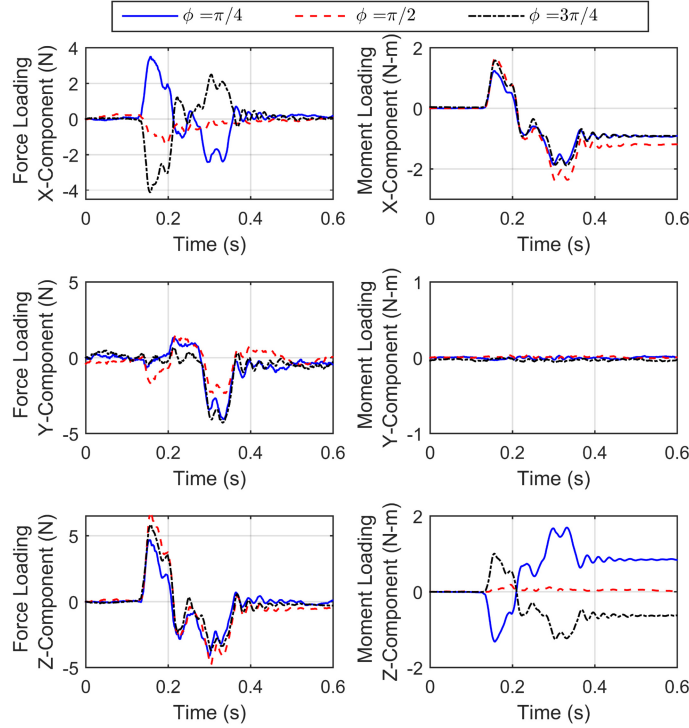


Fig. 12. Experimentally measured loading profiles for various roll angles.

## 7. BIPED STABILIZATION AND MANEUVERING

This section demonstrates the effectiveness of the DMST onboard a biped robot where the tail is used for pitch-angle disturbance rejection while standing and stabilization to enable a quasi-static walking gait. Two methods of analyzing the system will be presented: an analytical model implemented in MATLAB for the pitch-angle disturbance rejection, and a model generated in a multi-body dynamics software package for stabilization.

### 7.1 Pitch-Angle Disturbance Rejection

Figure 13 shows the DMST mounted vertically on a biped robot constructed of a pair of planar, two-DOF leg mechanisms developed by the authors<sup>16, 17</sup>. Figure 14 shows the schematic diagram of the system. The y-axis of the DMST aligns with the y-axis of the biped-fixed frame  $B$ , and the x-axes of these frames are aligned when the tail roll  $\phi = 0^\circ$ . Subscript  $B$  denotes vectors or matrices defined in the biped frame of reference. To model the pitching behavior of the robot in the  $+z_B$  direction, a revolute joint between the ground and rear foot contact is prescribed at frame  $J$ , where  $z_J$  is the axis of rotation of the joint.

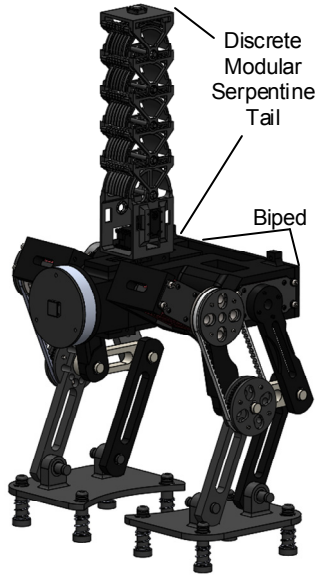


Fig. 13. Bipedal robot with vertically mounted DMST.

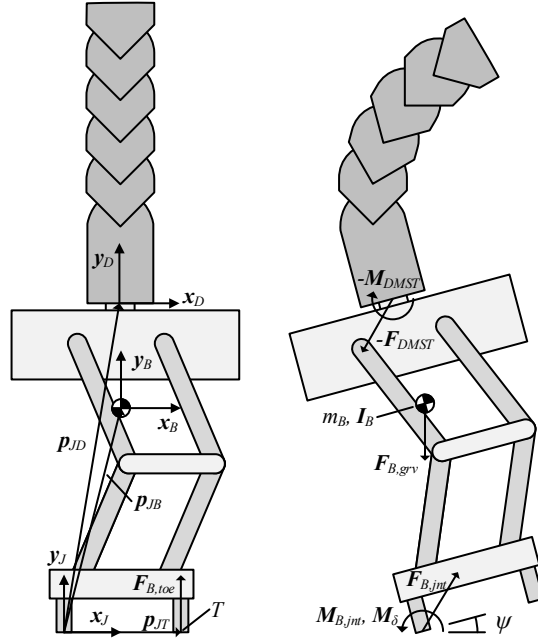


Fig. 14. Schematic diagram showing the biped and tail frame definitions, kinematic parameters and system loading.

This analysis will study how the tail can actively prevent the biped from tipping over. The system will be modeled as two-bodies consisting of a tail capable of producing pitch bending motions and a stationary biped robot. The kinematics of the system are defined with respect to the ground fixed frame  $J$  in Fig. 14. The pitch of the system is defined by the angle  $\psi$ , and the orientation of the biped-fixed frame  $B$  is defined by  $\mathbf{R}_B$  in Eq. 21, along with the biped's angular velocity. Three points at which loading is applied on the biped are located at the COM position (the origin of frame  $B$ ), the DMST frame  $D$  origin, and the forward toe contact point  $T$ . In the biped frame, the position vectors from the origin of frame  $J$  to the origins of frames  $B$  ( $\mathbf{p}_{JB,lcl}$ ) and  $D$  ( $\mathbf{p}_{JD,lcl}$ ) are fixed, and their definition in the global frame  $J$  may be found using Eq. 22. The position  $\mathbf{p}_{JT}$  is fixed in the global frame and will be prescribed based on the foot geometry.

$$\mathbf{R}_B = \mathbf{R}_Z(\psi), \quad \boldsymbol{\omega}_B = \dot{\psi} \mathbf{z} \quad (21)$$

$$\mathbf{p}_{JB} = \mathbf{R}_B \mathbf{p}_{JB,lcl}, \quad \mathbf{p}_{JD} = \mathbf{R}_B \mathbf{p}_{JD,lcl} \quad (22)$$

Furthermore, due to the motion of frame  $D$  fixed to the biped, the formulations for several kinematic parameters defined in section 4.2 need to be modified for this analysis. Equation 23 defines modifications for the link 0 orientation  $\mathbf{R}_{D,0}$  from Eq. 6, the link 0 angular velocity  $\boldsymbol{\omega}_{D,0}$  from Eq. 9, and the joint 0 position  $\mathbf{p}_{D,jnt,0}$  from Eq. 7.

$$\mathbf{R}_{D,0} = \mathbf{R}_B \mathbf{R}_Y(\phi), \quad \boldsymbol{\omega}_{D,0} = \boldsymbol{\omega}_B + \dot{\phi} \mathbf{R}_{D,0} \mathbf{y}, \quad \mathbf{p}_{D,jnt,0} = \mathbf{p}_{JD} \quad (23)$$

The loading associated with the tail ( $-\mathbf{F}_{DMST}$  and  $-\mathbf{M}_{DMST}$ ), joint ( $\mathbf{F}_{B,jnt}$  and  $\mathbf{M}_{B,jnt}$ ), toe ( $\mathbf{F}_{B,toe}$ ), gravity ( $\mathbf{F}_{B,grv}$ ) and disturbance ( $\mathbf{M}_\delta$ ) are shown in Fig. 14. The disturbance moment  $\mathbf{M}_\delta$  represents a generalized disturbance to the system, such as an impact force on the body of the biped robot, or an unexpected shift in height of the ground. Loading equal and opposite to the DMST loading from section 5 is applied to the biped at the origin of frame  $D$  as the control input to the system. When  $\psi = 0^\circ$ , the forward toes of the leg will be in contact with the ground, generating a force to prevent the pitch angle from becoming negative. In addition to the gravitational loading from the tail incorporated into  $\mathbf{F}_{DMST}$  and  $\mathbf{M}_{DMST}$ , a gravitational force  $\mathbf{F}_{B,grv}$  is also applied at the biped COM. Finally,  $\mathbf{F}_{B,jnt}$  and  $\mathbf{M}_{B,jnt}$  act at the revolute joint to counteract loading other than pitch angle rotation. For  $\mathbf{F}_{B,jnt}$ , all three components can be non-zero to ensure equilibrium, and  $\mathbf{M}_{B,jnt}$  can be non-zero in the  $x$ - $y$  plane of frame  $J$ . The  $z$ -component of  $\mathbf{M}_{B,jnt}$  must be zero, since the  $z$ -axis is the revolute joint axis and a revolute joint by definition cannot support a constraint moment about its joint axis.

The force and moment equilibria of the system taken with respect to the biped COM is defined in Eq. 24, where  $\mathbf{I}_B$  is the biped moment of inertia and the vectors  $\mathbf{p}_{BJ}$  and  $\mathbf{p}_{BD}$  are the position vectors from the frame  $B$  origin to frames  $J$  and  $D$  respectively.

$$\begin{aligned} m_B \ddot{\mathbf{p}}_{JB} &= \mathbf{F}_{B,jnt} + \mathbf{F}_{B,toe} + \mathbf{F}_{B,grv} - \mathbf{F}_{DMST} \\ \mathbf{I}_B \dot{\boldsymbol{\omega}}_B + \tilde{\boldsymbol{\omega}}_B \mathbf{I}_B \boldsymbol{\omega}_B &= \mathbf{M}_\delta + \mathbf{M}_{B,jnt} + \tilde{\mathbf{p}}_{BJ} \mathbf{F}_{B,jnt} + \tilde{\mathbf{p}}_{BF} \mathbf{F}_{B,toe} - \mathbf{M}_{DMST} - \tilde{\mathbf{p}}_{BD} \mathbf{F}_{DMST} \end{aligned} \quad (24)$$

The moment equation may be reformulated in relation to point  $J$  to utilize the vectors  $\mathbf{p}_{JC}$ ,  $\mathbf{p}_{JD}$  and  $\mathbf{p}_{JT}$ , as shown in Eq. 25.

$$\begin{aligned} (\mathbf{I}_B - m_B \tilde{\mathbf{p}}_{JB} \tilde{\mathbf{p}}_{JB}) \dot{\boldsymbol{\omega}}_B + \tilde{\boldsymbol{\omega}}_B (\mathbf{I}_B - m_B \tilde{\mathbf{p}}_{JB} \tilde{\mathbf{p}}_{JB}) \boldsymbol{\omega}_B \\ = \mathbf{M}_\delta + \mathbf{M}_{B,jnt} + \tilde{\mathbf{p}}_{JF} \mathbf{F}_{B,toe} + \tilde{\mathbf{p}}_{JB} \mathbf{F}_{B,grv} - \tilde{\mathbf{p}}_{JD} \mathbf{F}_{DMST} - \mathbf{M}_{DMST} \end{aligned} \quad (25)$$

Table IV and Eq. 26 define the properties of the biped and DMST designs extracted from the CAD model shown in Fig. 13 used in these simulations. A 3.5 kg proof mass is added to the terminal link of the tail such that  $\beta = 0.8$ , as shown in the definition of  $m_{D,5}$ , to provide the tail with sufficient loading capacity to affect the biped dynamics.

Table IV. Simulation parameters for biped with DMST.

Property	Value	Property	Value
$\mathbf{p}_{JB,icl}$	[96.4; 336.9; 0] mm	$m_B$	9.525 kg
$\mathbf{p}_{JD,icl}$	[52.8; 497.2; 0] mm	$m_{D,0}$	0.350 kg
$\mathbf{p}_{JT}$	[190.0; 0; 0] mm	$m_{D,\{1-4\}}$	0.267 kg
$L_{J2C,0}$	63.3 mm	$m_{D,5}$	3.5 kg
$L_{J2C}$	59 mm	$L_{J2J,0}$	105.25 mm
$L_{J2C,n}$	49 mm	$L_{J2J}$	60 mm
$r_i$	[9, 16, 22, 28, 34] mm	$R$	25 m

$$\mathbf{I}_{B,icl} = \begin{bmatrix} 0.3929 & -0.0142 & 0 \\ -0.0142 & 0.2782 & 0 \\ 0 & 0 & 0.2780 \end{bmatrix} \text{ kg-m}^2 \quad (26)$$

In this simulation, only the gravitational loading effects of the tail are taken into consideration; the effect of the inertia dynamics in the control problem remains as an element of future work. A controller is designed to modify the bending of the tail in response to undesirable pitch angle displacement and velocity. For a given tail, there will be a motor angle  $\theta_{m,max}$  that corresponds to the tail configuration that generates the maximum pitch gravitational moment with respect to the tail frame  $B$ . For the tail under consideration, this will occur when the sum of the joint angles  $\theta_1$  through  $\theta_5$  is  $90^\circ$ . Using Eq. 4 and the parameters in Table IV,  $\theta_{m,max} = 64.29^\circ$ . The controller should modify  $\theta_m$  within the range of  $[-\theta_{m,max}, \theta_{m,max}]$  based on the biped pitch angle and pitch angular velocity. Equation 27 defines the control law for  $\theta_m$ , with  $\phi$  fixed at  $0^\circ$ , where  $u_m$  defines the direction and intensity of the control action,  $K_p$  (unitless) and  $K_v$  (units: sec) are non-dimensionalizing gains for the pitch angle and pitch angular velocity with units rad and rad/s, respectively, and ‘sat’ is the unit saturation function, such that  $u_m$  falls within  $[-1, 1]$ . In this simulation,  $K_p = 10$  and  $K_v = 1$  sec.

$$\theta_m = \theta_{m,max} u_m \quad u_m = -\text{sat}(K_p \psi + K_v \dot{\psi}) \quad (27)$$

Figure 15 shows the behavior of the system with and without compensation from the tail for a disturbance  $\mathbf{M}_\delta$  defined by Eq. 28, where  $M_{\delta,mag} = 15$  N-m and  $\Delta t = 0.5$  sec. Without tail compensation, the destabilizing moment is sufficient to tip the COM over the revolute joint, fully destabilizing the system, starting at  $M_{\delta,mag} = 14.7$  N-m.

For  $M_{\delta, mag} = 15$  N-m, with tail compensation, the tail bends forward in the  $-\psi$  direction, compensating for the destabilizing moment in the  $+\psi$  direction. This motion modifies the tail's loading applied to the biped in  $\mathbf{M}_{DMST}$  such that the disturbance only causes a slight pitch of the system before it falls back to a stable configuration. For the gains  $K_p$  and  $K_v$  chosen, the maximum magnitude of  $u_m$  is -0.411; meaning that the controller did not have to drive the tail to its maximum position in order to stabilize for this disturbance.

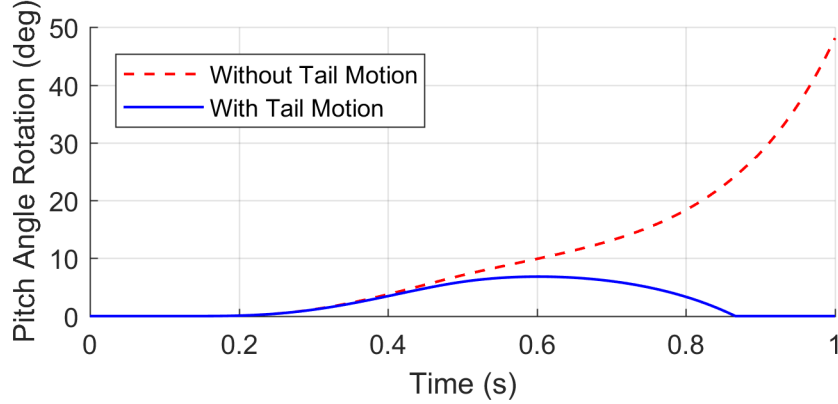


Fig. 15. Pitch angle stabilization of the biped with DMST.

$$\mathbf{M}_{\delta} = \begin{cases} M_{\delta, mag} \sin(\pi t / \Delta t) & 0 \leq t \leq \Delta t \\ 0 & t > \Delta t \end{cases} \quad (28)$$

The maximum disturbance magnitude these control gains can accommodate is 20.4 N-m, representing a 39% increase in maximum allowable disturbance magnitude with respect with the destabilizing moment of 14.7 N-m. If the tail is held fixed at  $\theta_m = -\theta_{m, max}$  throughout the full simulation, the maximum disturbance magnitude it can accommodate is  $M_{\delta, mag} = 24.8$  N-m, which represents the theoretical maximum disturbance this tail can reject based on gravitational loading given the biped and tail geometry and mass distribution. Future work will provide a more focused analysis on the controls aspects of this research, including formulating torque-based control laws for the motors, instead of position-based set points, and analyzing additional factors that may be used to improve system control, such as using contact force measurements in the feet to aid in tail positioning to detect disturbances before they manifest in pitching motion.

## 7.2 Gait Stabilization

In this section, dynamics simulations are performed to investigate the proposed mechanism's ability to stabilize the robotic system shown in Fig. 13 during a walking gait. The Solidworks CAD model of the robotic system was exported to MSC ADAMS<sup>63</sup>, a physics-based multi-body dynamics simulation software. ADAMS is able to calculate the absolute motions of all bodies subject to torques applied on the joints by virtual actuators while taking into account the mass, inertia, body accelerations and contact/frictional forces between the feet and ground.

As a preliminary investigation into gait stabilization, the robotic system's COM is used as a stability criteria to calculate the tail trajectory required to stabilize the biped robot during a walking gait. This criteria states that the horizontal projection of the COM should fall within the biped robot's support polygon defined as the convex hull generated by the contact points of the feet to ensure a stable quasi-static walking gait<sup>64</sup>. To evaluate this criteria, Eqs. 8 and 22 are used to compute the robotic systems COM,  $\mathbf{p}_{COM}$ , given by Eq. 29.

$$\begin{aligned} \mathbf{p}_{T, COM, lcl} &= \frac{\sum_{i=0}^n m_{D, i} \mathbf{p}_{D, COM, i}}{m_T}, \\ m_T &= m_{D, 0} + \sum_{i=1}^n m_{D, i}, \quad \mathbf{p}_{T, COM} = \mathbf{p}_{JD} + \mathbf{R}_B \mathbf{p}_{T, COM, lcl}, \\ \mathbf{p}_{COM} &= \frac{m_B \mathbf{p}_{JB} + m_T \mathbf{p}_{T, COM}}{m_B + m_T} \end{aligned} \quad (29)$$

As discussed in section 7.1, the largest displacements of tail COM away from its base occurs at  $\theta_{m, max} = \pm 64.29^\circ$ . Using simulation parameters presented in Table IV, rotating the tail by  $\pm \theta_{m, max}$  approximately centers  $\mathbf{p}_{COM}$  within the single support polygon of the left and right foot. The roll DOF was used to keep  $\mathbf{p}_{COM}$  within the

single support polygon as the robot performs a walking gait with a 150 mm step length. Figure 16 depicts the dynamic simulation of the biped robot performing a stable quasi-static forward walking gait enabled by the DMST. The biped provides forward propulsive motion during the single support phases with the tail swung over the left or right foot, shown in Figs. 16 (a, c) and alternates between the two configurations during the double support phase as shown in Fig. 16 (b). Future work will build upon this analysis to account for the inertial loading to enable stabilization of dynamic gaits.

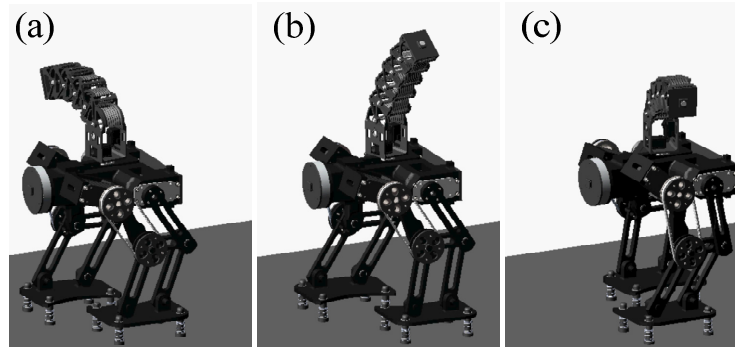


Fig. 16. Dynamic simulation depicting the DMST stabilizing a planar biped robot performing a quasi-static stable forward walking gait: (a) left support phase, (b) double support phase, and (c) right single support phase.

## 8. CONCLUSION AND FUTURE WORK

This paper presented the design, analysis and experimentation of an articulated, spatial robotic tail that is envisioned for use on board a legged mobile robot to serve as an external source of loading separate from the legs for enhanced maneuvering and stabilization. The proposed mechanism utilizes a serpentine-like structure actuated via a cable transmission system with a cylindrical cable routing method that maintains equal and opposite antagonistic cable displacements. Kinematic and dynamic models were developed and validated by a series of case studies and experiments using a five-link DMST prototype. Experimental results indicate that the proposed mechanism exhibits satisfactory accuracy and repeatability where the largest recorded angular orientation error was  $3.1^\circ$  and standard deviation was  $\pm 0.8^\circ$ . Measured dynamic loading profiles closely match the behavior of analytically computed case studies as the roll angle is varied; variations result from vibrations induced in the long tail structure and internal friction that slightly reduced the response time of the tail motions. The prototype can produce maximum spatial force and moment loading equal to 6 N and 1.8 N-m.

The analysis in this paper will be used to design robotic tails by using results to select trajectory and design properties to produce required tail loading profiles. Future work involves the redesign and miniaturization of the tail structural components manufactured from metal to enable the integration of high power dc motors to increase magnitudes of dynamic loading profiles. Design features to improve the flexibility and increase the workspace of the mechanism will be considered to investigate the manipulation capabilities of serially connected DMSTs. Further analysis and dynamic models will be developed to analytically determine the effects of spatial tail motions on a legged robot and control laws will be derived for stabilization, maneuvering and dynamic self-righting. The multi-body dynamic simulation will be further developed to enable hardware-in-the-loop simulations of a virtual legged robot that utilizes real-time measurements of loading profiles generated by the prototype to conduct various case studies and validate dynamic models and control laws.

## ACKNOWLEDGEMENTS

This material is based upon work supported by the National Science Foundation under Grant No. 1557312.

## REFERENCES

1. G. C. Hickman, "The mammalian tail: a review of functions," *Mammal Review* **9**(4), 143-157 (1979).
2. U. Proske, "Energy conservation by elastic storage in kangaroos," *Endeavour* **4**(4), 148-153 (1980).
3. A. B. Howell, "Speed in animals, their specialization for running and leaping," *American Journal of Physical Anthropology* **3**(1), 109-110 (1944).
4. M. J. Benton, "Studying function and behavior in the fossil record," *PLoS Biology* **8**(3), e1000321 (2010).
5. T. Libby, T. Y. Moore, E. Chang-Siu, D. Li, D. J. Cohen, A. Jusufi and R. J. Full, "Tail-assisted pitch control in lizards, robots and dinosaurs," *Nature* **481**(7380), 181-184 (2012).
6. A. Jusufi, D. Kawano, T. Libby and R. Full, "Righting and turning in mid-air using appendage inertia: reptile tails, analytical models and bio-inspired robots," *Bioinspiration and Biomimetics* **5**(4), 045001 (2010).
7. S. Kajita and B. Espiau, Springer handbook of robotics. pp. 361-389 (Springer-Verlag Berlin Heidelberg, 2008).
8. W. Saab and P. Ben-Tzvi, "Design and Analysis of a Discrete Modular Serpentine Robotic Tail for Improved Performance of Mobile Robots," **In: International Design Engineering Technical Conferences and Computers and Information in Engineering Conference** (2016) pp. V05AT07A061.
9. W. S. Rone and P. Ben-Tzvi, "Continuum Manipulator Statics Based on the Principle of Virtual Work," **In: International Mechanical Engineering Congress and Exposition** (2012) pp. 321-328.
10. W. S. Rone and P. Ben-Tzvi, "Multi-Segment Continuum Robot Shape Estimation Using Passive Cable Displacement," **In: International Symposium on Robotic and Sensors Environments** (2013) pp. 37-42.
11. W. S. Rone and P. Ben-Tzvi, "Continuum Robotic Tail Loading Analysis for Mobile Robot Stabilization and Maneuvering," **In: International Design Engineering Technical Conferences and Computers and Information in Engineering Conference** (2014) pp. V05AT08A009-V005AT008A009.
12. W. S. Rone and P. Ben-Tzvi, "Mechanics modeling of multisegment rod-driven continuum robots," *ASME Journal of Mechanisms and Robotics* **6**(4), 041006 (2014).
13. W. S. Rone and P. Ben-Tzvi, "Continuum robot dynamics utilizing the principle of virtual power," *IEEE Transactions on Robotics* **30**(1), 275-287 (2014).
14. W. S. Rone and P. Ben-Tzvi, "Static Modeling of a Multi-Segment Serpentine Robotic Tail," **In: International Design Engineering Technical Conferences and Computers and Information in Engineering Conference** (2015) pp. V05AT08A054-V005AT008A054.
15. W. S. Rone and P. Ben-Tzvi, "Dynamic modeling and simulation of a yaw-angle quadruped maneuvering with a planar robotic tail," *ASME Journal of Dynamic Systems Measurement and Control* **138**(8), DS-15-1456 (2016).
16. W. Saab and P. Ben-Tzvi, "Design and Analysis of a Robotic Modular Leg," **In: International Design Engineering Technical Conference and Computers and Information in Engineering Conference** (2016) pp. V05AT07A062.
17. W. Saab, W. Rone and P. Ben-Tzvi, "Robotic modular leg: design, analysis and experimentation," *Journal of Mechanisms and Robotics* **9**(2), 024501-024501-024506 (2017).
18. J. R. Wertz, *Spacecraft attitude determination and control*, (Springer Science & Business Media, 2012).
19. G. C. Oates, *Aircraft propulsion systems technology and design*, (Aiaa, 1989).
20. S.-H. Lee and A. Goswami, "Reaction Mass Pendulum (RMP): An Explicit Model for Centroidal Angular Momentum of Humanoid Robots," **In: IEEE International Conference on Robotics and Automation** (2007) pp. 4667-4672.
21. M. D. Carpenter and M. A. Peck, "Reducing base reactions with gyroscopic actuation of space-robotic systems," *IEEE Transactions on Robotics* **25**(6), 1262-1270 (2009).
22. S. Ge and H. Cheng, "A Comparative Design of Satellite Attitude Control System with Reaction Wheel," **In: First NASA/ESA Conference on Adaptive Hardware and Systems** (2006) pp. 359-364.
23. K. Machairas and E. Papadopoulos, "On Quadruped Attitude Dynamics and Control Using Reaction Wheels and Tails," **In: European Control Conference** (2015) pp. 753-758.
24. G.-H. Liu, H.-Y. Lin, H.-Y. Lin, S.-T. Chen and P.-C. Lin, "A bio-inspired hopping kangaroo robot with an active tail," *Journal of Bionic Engineering* **11**(4), 541-555 (2014).
25. G. He and Z. Geng, "Exponentially stabilizing an one-legged hopping robot with non-SLIP model in flight phase," *Mechatronics* **19**(3), 364-374 (2009).
26. E. Chang-Siu, T. Libby, M. Tomizuka and R. J. Full, "A lizard-inspired active tail enables rapid maneuvers and dynamic stabilization in a terrestrial robot," **In: 2011 IEEE/RSJ International Conference on Intelligent Robots and Systems** (2011) pp. 1887-1894.
27. A. Patel and M. Braae, "Rapid Acceleration and Braking: Inspirations from the Cheetah's Tail," **In: IEEE International Conference on Robotics and Automation** (2014) pp. 793-799.
28. N. Kohut, D. Haldane, D. Zarrouk and R. Fearing, "Effect of Inertial Tail on Yaw Rate of 45 Gram Legged Robot," **In: International Conference on Climbing and Walking Robots and the Support Technologies for Mobile Machines** (2012) pp. 157-164.
29. A. Patel and M. Braae, "Rapid Turning at High-Speed: Inspirations from the Cheetah's Tail," **In: IEEE/RSJ International Conference on Intelligent Robots and Systems** (2013) pp. 5506-5511.
30. V. Kopman, J. Laut, F. Acquaviva, A. Rizzo and M. Porfiri, "Dynamic modeling of a robotic fish propelled by a compliant tail," *IEEE Journal of Oceanic Engineering* **40**(1), 209-221 (2015).

31. F. J. Berenguer and F. M. Monasterio-Huelin, "Zappa, a quasi-passive biped walking robot with a tail: Modeling, behavior, and kinematic estimation using accelerometers," *IEEE Transactions on Industrial Electronics* **55**(9), 3281-3289 (2008).
32. R. Briggs, J. Lee, M. Haberland and S. Kim, "Tails in Biomimetic Design: Analysis, Simulation, and Experiment," **In: IEEE/RSJ International Conference on Intelligent Robots and Systems** (2012) pp. 1473-1480.
33. E. Chang-Siu, T. Libby, M. Brown, R. J. Full and M. Tomizuka, "A Nonlinear Feedback Controller for Aerial Self-Righting by a Tailed Robot," **In: International Conference on Robotics and Automation** (2013) pp. 32-39.
34. A. Mutka, M. Orsag and Z. Kovacic, "Stabilizing a Quadruped Robot Locomotion using a Two Degree of Freedom Tail," **In: 21st Mediterranean Conference on Control & Automation** (2013) pp. 1336-1342.
35. L. Birglen, T. Laliberté and C. M. Gosselin, *Underactuated robotic hands*, (Springer, 2007).
36. R. Balasubramanian and A. M. Dollar, "A Framework for Studying Underactuation in the Human Hand," **In: Annual Meeting of the American Society of Biomechanics** (2010) pp. 5-6.
37. W. M. Kier and K. K. Smith, "Tongues, tentacles and trunks: the biomechanics of movement in muscular-hydrostats," *Zoological Journal of the Linnean Society* **83**(4), 307-324 (1985).
38. G. Robinson and J. B. C. Davies, "Continuum Robots-A State of the Art," **In: International Conference on Robotics and Automation** (1999) pp. 2849-2854.
39. W. McMahan, B. A. Jones and I. D. Walker, "Design and Implementation of a Multi-Section Continuum Robot: Air-Octor," **In: IEEE/RSJ International Conference on Intelligent Robots and Systems** (2005) pp. 2578-2585.
40. B. Tondu and P. Lopez, "The McKibben muscle and its use in actuating robot-arms showing similarities with human arm behaviour," *Industrial Robot: An International Journal* **24**(6), 432-439 (1997).
41. B. Mazzolai, L. Margheri, M. Cianchetti, P. Dario and C. Laschi, "Soft-robotic arm inspired by the octopus: II. From artificial requirements to innovative technological solutions," *Bioinspiration and Biomimetics* **7**(2), 025005 (2012).
42. N. Simaan, R. Taylor and P. Flint, "A Dexterous System for Laryngeal Surgery," **In: International Conference on Robotics and Automation** (2004) pp. 351-357.
43. H. Tsukagoshi, A. Kitagawa and M. Segawa, "Active Hose: An Artificial Elephant's Nose With Maneuverability For Rescue Operation," **In: International Conference on Robotics and Automation** (2001) pp. 2454-2459.
44. A. Wolf, H. B. Brown, R. Casciola, A. Costa, M. Schwerin, E. Shamas and H. Choset, "A Mobile Hyper Redundant Mechanism for Search and Rescue Tasks," **In: IEEE/RSJ International Conference on Intelligent Robots and Systems** (2003) pp. 2889-2895.
45. K.-W. Kwok, G. P. Mylonas, L. W. Sun, M. Lerotic, J. Clark, T. Athanasiou, A. Darzi and G.-Z. Yang, "Dynamic Active Constraints for Hyper-Redundant Flexible Robots," **In: Medical Image Computing and Computer-Assisted Intervention** (2009) pp. 410-417.
46. Y.-J. Kim, S. Cheng, S. Kim and K. Iagnemma, "A stiffness-adjustable hyperredundant manipulator using a variable neutral-line mechanism for minimally invasive surgery," *IEEE Transactions on Robotics* **30**(2), 382-395 (2014).
47. M. Cianchetti, F. Renda, A. Licofonte and C. Laschi, "Sensorization of continuum soft robots for reconstructing their spatial configuration," **In: 4th IEEE RAS & EMBS International Conference on Biomedical Robotics and Biomechatronics** (2012) pp. 634-639.
48. G. Granosik, J. Borenstein and M. G. Hansen, *Serpentine Robots for Industrial Inspection and Surveillance*, (Citeseer, 2006).
49. C. Wright, A. Buchan, B. Brown, J. Geist, M. Schwerin, D. Rollinson, M. Tesch and H. Choset, "Design and Architecture of the Unified Modular Snake Robot," **In: International Conference on Robotics and Automation** (2012) pp. 4347-4354.
50. H. Date and Y. Takita, "Adaptive Locomotion of a Snake Like Robot Based on Curvature Derivatives," **In: IEEE/RSJ International Conference on Intelligent Robots and Systems** (2007) pp. 3554-3559.
51. A. Maity and S. Majumder, "Serpentine Robots: A Study of Design Philosophy," **In: International Conference on Advanced Robotics** (2011) pp. 549-555.
52. Z. Li and R. Du, "Design and analysis of a bio-inspired wire-driven multi-section flexible robot," *International Journal of Advanced Robotic Systems* **10**, (2013).
53. Z. Li, R. Du, M. C. Lei and S. M. Yuan, "Design and Analysis of a Biomimetic Wire-Driven Robot Arm," **In: ASME International Mechanical Engineering Congress and Exposition** (2011) pp. 191-198.
54. Z. Li, R. Du, H. Yu and H. Ren, "Statics Modeling of an Underactuated Wire-Driven Flexible Robotic Arm," **In: 5th IEEE RAS/EMBS International Conference on Biomedical Robotics and Biomechatronics** (2014) pp. 326-331.
55. J.-w. Suh, K.-y. Kim, J.-w. Jeong and J.-j. Lee, "Design considerations for a hyper-redundant pulleyless rolling joint with elastic fixtures," *IEEE/ASME Transactions on Mechatronics* **20**(6), 2841-2852 (2015).
56. S. C. Jacobsen, E. K. Iversen, D. F. Knutti, R. T. Johnson and K. B. Biggers, "Design of the Utah/MIT Dexterous Hand," **In: International Conference on Robotics and Automation** (1986) pp. 1520-1532.
57. C. S. Loucks, V. J. Johnson, P. T. Boissiere, G. P. Starr and J. P. Steele, "Modeling and Control of the Stanford/JPL Hand," **In: International Conference on Robotics and Automation** (1987) pp. 573-578.
58. S. Hirose and Y. Umetani, "The development of soft gripper for the versatile robot hand," *Mechanism and Machine Theory* **13**(3), 351-359 (1978).
59. M. G. Catalano, G. Grioli, E. Farnioli, A. Serio, C. Piazza and A. Bicchi, "Adaptive synergies for the design and control of the Pisa/IIT SoftHand," *The International Journal of Robotics Research* **33**(5), 768-782 (2014).

60. G. Palli, "Model and control of tendon actuated robots," (2007).
61. R. Ozawa, H. Kobayashi and K. Hashirii, "Analysis, classification, and design of tendon-driven mechanisms," *IEEE Transactions on Robotics* **30**(2), 396-410 (2014).
62. E. Colgate and N. Hogan, "An Analysis of Contact Instability in Terms of Passive Physical Equivalents," **In:** *IEEE International Conference on Robotics and Automation* (1989) pp. 404-409.
63. M. S. Corporation, "Msc Adams ", (2005).
64. R. B. McGhee and A. A. Frank, "On the stability properties of quadruped creeping gaits," *Mathematical Biosciences* **3**, 331-351 (1968).